RESEARCH ARTICLE

R2* and quantitative susceptibility mapping in deep gray matter of 498 healthy controls from 5 to 90 years

Sarah Treit [ORCID] | Nashwan Naji | Peter Seres | Julia Rickard | Emily Stolz | Alan H. Wilman | Christian Beaulieu

Department of Biomedical Engineering, Faculty of Medicine & Dentistry, University of Alberta, Edmonton, Alberta, Canada

Correspondence
Sarah Treit, 1098 Research Transition Facility, Department of Biomedical Engineering, University of Alberta, Edmonton, Alberta, Canada T6G 2V2.
Email: treit@ualberta.ca

Abstract

Putative MRI markers of iron in deep gray matter have demonstrated age related changes during discrete periods of healthy childhood or adulthood, but few studies have included subjects across the lifespan. This study reports both transverse relaxation rate (R2*) and quantitative susceptibility mapping (QSM) of four primary deep gray matter regions (thalamus, putamen, caudate, and globus pallidus) in 498 healthy individuals aged 5–90 years. In the caudate, putamen, and globus pallidus, increases of QSM and R2* were steepest during childhood continuing gradually throughout adulthood, except caudate susceptibility which reached a plateau in the late 30s. The thalamus had a unique profile with steeper changes of R2* (reflecting additive effects of myelin and iron) than QSM during childhood, both reaching a plateau in the mid-30s to early 40s and decreasing thereafter. There were no hemispheric or sex differences for any region. Notably, both R2* and QSM values showed more inter-subject variability with increasing age from 5 to 90 years, potentially reflecting a common starting point in iron/myelination during childhood that diverges as a result of lifestyle and genetic factors that accumulate with age.

KEYWORDS
aging, brain iron, deep gray matter, development, lifespan, R2*, susceptibility

1 | INTRODUCTION

Non-heme iron is essential for several key neuronal and glial functions in the brain, including DNA synthesis, enzyme, and neurotransmitter function and the formation of myelin (Rouault, 2013; Ward, Zucca, Duyn, Crichton, & Zecca, 2014). Iron deficiency in early life impairs brain development (Beard, 2003; Lozoff & Georgieff, 2006), while iron overload in older adults causes oxidative stress and fosters neurodegeneration (Mills, Dong, Wang, & Xu, 2010), suggesting that a critical balance of iron is necessary for normal brain function

throughout the lifespan. Several mechanisms are involved in regulating iron homeostasis, including via the blood brain barrier (Fillebeen et al., 1999; Moos, Rosengren Nielsen, Skjørringe, & Morgan, 2007); however, the capacity for iron regulation declines with age leading to iron deposits that accumulate over time (Farrall & Wardlaw, 2009).

Autopsy studies of previously healthy subjects indicate that iron is unevenly distributed in the brain, with the highest concentration found in the basal ganglia and the lowest in the cortex, increasing with age at varying rates across structures (Hallgren & Sourander, 1958; Ramos et al., 2014). In the basal ganglia, iron increases level off in early adulthood, remaining constant or continuing only gradually across the remainder of the lifespan, while iron in the thalamus

Sarah Treit and Nashwan Naji are co-first author.

increases during development and then decreases after approximately 35 years of age (Hallgren & Sourander, 1958). Autopsy studies also demonstrate that deep gray matter structures undergo myelination in early development, starting first in the globus pallidus and thalamus followed by the caudate and putamen (Hasegawa et al., 1992), which serves to increase the conduction velocity of action potentials and enhance communication across brain networks.

Several quantitative MRI methods are sensitive to both brain iron and myelin including the transverse relaxation rate R2*, and quantitative susceptibility mapping (QSM) (Haacke et al., 2005; Schenck & Zimmerman, 2004; Wang & Liu, 2015). Both R2* and QSM have demonstrated good reproducibility (Feng, Deistung, & Reichenbach, 2018; Spincemaille et al., 2019) and strong correlations with postmortem iron measures (Langkammer et al., 2010; Langkammer et al., 2012; Sun et al., 2015). These techniques suggest that excess iron accumulation or loss is associated with various neurodevelopmental (e.g., ADHD—Cortese et al., 2012; autism—Tang et al., 2020) and neurodegenerative disorders (e.g., Parkinson's disease, Huntington's disease, Multiple Sclerosis, and dementia; for review see Wang et al., 2017). In healthy subjects, studies have demonstrated correlations between R2* or QSM of basal ganglia structures and various aspects of brain function including working memory in children and adults (Darki, Nemmi, Möller, Sitnikov, & Klingberg, 2016) processing speed (Hect, Daugherty, Hermez, & Thomason, 2018) and IQ in children (Carpenter et al., 2016; Hect et al., 2018), cognitive switching (Daugherty, Hoagey, Kennedy, & Rodrigue, 2019), executive function, and psychomotor speed in adults (Ghadery et al., 2015). Further, a recent large longitudinal study demonstrated a relationship between longitudinal increases of R2* of the putamen during late adolescence and superior overall cognitive performance (Larsen et al., 2020). Correlations between putative measures of brain iron and cognition across wider age-spans of subjects would contribute to an understanding of the functional relevance of changes in these measures.

Putative age-related changes of iron in deep gray matter during healthy development and aging have mostly been reported using only R2* (Aquino et al., 2009; Daugherty et al., 2019; Daugherty & Raz, 2016; Ghadery et al., 2015; Haacke et al., 2010; Hect et al., 2018; Larsen et al., 2020; Pirpamer et al., 2016) or only QSM (Acosta-Cabronero, Betts, Cardenas-Blanco, Yang, & Nestor, 2016; Bilgic, Pfefferbaum, Rohlfing, Sullivan, & Adalsteinsson, 2012; Carpenter et al., 2016; Darki et al., 2016; Gong, Wong, Hui, Chan, & Leung, 2015; Li et al., 2020; Ning et al., 2019; Persson et al., 2015; Zhang et al., 2019) in discrete age groups (only children or only adults, with two exceptions: R2* 1–80 years, $n = 80$—Aquino et al., 2009; QSM, 1–81 years, $n = 191$—Zhang et al., 2018). Only a limited number of studies have reported both QSM and R2* in deep gray matter of healthy populations, and include studies of infants (Zhang et al., 2019), adolescents (Peterson et al., 2019) or adults (Betts, Acosta-Cabronero, Cardenas-Blanco, Nestor, & Düzel, 2016). Only one study using both R2* and QSM included participants across the lifespan ($n = 191$, 1–81 years); demonstrating steep increases of both R2* and QSM in the first few years of life followed by slower but steady increases varying across six deep gray matter structures

(Li et al., 2014). No sex differences in R2* or QSM of deep gray matter were found, in agreement with some (Hect et al., 2018), but not others (Gong et al., 2015; Persson et al., 2015; Peterson et al., 2019), while most studies did not test for sex differences presumably due to small sample sizes. In addition, the majority of these studies present results combined across hemisphere (e.g., Acosta-Cabronero et al., 2016; Li et al., 2014; Zhang et al., 2019), while some smaller studies have suggested subtle differences in measures of brain iron between left and right counterparts of gray matter structures (e.g., Gong et al., 2015) and others present left and right data separately without directly testing for differences (e.g., Tullo et al., 2019). Given that the effects of sex and hemisphere remain unclear and may differ with age, testing for sex and hemispheric differences in a large sample spanning a wide age range is warranted.

R2* and QSM presumably provide complementary information given that both increase with iron, while myelin elevates R2* but decreases QSM. However, studies including both measures in the same sample have typically compared R2* and QSM using linear correlations, pooled across structures (e.g., Li et al., 2014; Peterson et al., 2019). Although this demonstrates a tight relationship between R2* and QSM, these correlations are potentially confounded by large differences in both susceptibility and R2* across structures, as well as the influence of age. This study proposes to convert R2* and QSM to Z scores to allow comparison on the same scale and test differences in fit parameters as a means to overcome these confounds.

The purpose of this study is to assess and compare QSM and R2* of four primary deep gray matter structures (caudate, putamen, globus pallidus and thalamus) versus age, sex, and cognitive scores in a cross-sectional sample of 498 healthy subjects over the ages of 5–90 years. These structures were chosen given their key roles in numerous developmental and neurodegenerative conditions, and their high reproducibility with automated segmentation methods. We hypothesize that R2* and QSM will increase with age following a pattern similar to that of previous autopsy work, including continued increases in the caudate, putamen and globus pallidus, and an inflection and subsequent decrease in the thalamus. R2* and QSM trajectories are expected to differ during periods of myelination (i.e., during development) in structures where myelin is most abundant (e.g., the thalamus).

2 | METHODS

2.1 | Participants

Five hundred and thirty-seven participants were recruited and scanned on the same 3T in the Peter S Allen MRI Research Centre at the University of Alberta as part of two studies on healthy brain development. Of these 537 subjects scanned, 38 were excluded for image quality and one was excluded for an incidental finding involving the basal ganglia, leaving 498 subjects included in the analysis here from 5 to 90 years (286 females 35 ± 21 years; 212 males 36 ± 22 years).

Participants were recruited through advertising or word of mouth, and were screened for self-reported history of developmental, psychiatric or neurological disorders, history of significant head injury, or contraindications to MRI. All participants provided written informed consent (in addition to written assent for participants under the age of 18) prior to enrollment, and both studies were approved by the Health Research Ethics Board at the University of Alberta.

2.2 | Cognitive assessment

All participants underwent a brief cognitive assessment using the NIH Cognition Toolbox (Gershon et al., 2010). Subtests included Picture Sequence Memory Task, Dimensional Card Sorting, List Sorting Working Memory, Rey Auditory Verbal Learning, and the Oral Symbol Digit Task to provide basic measures of memory, processing speed, and executive function. Standard (age corrected) scores were used for Picture Sequence Memory, Dimensional Card Sorting and List Sorting Working Memory, while this battery produces only raw scores for Oral Symbol Digit and Rey Auditory Verbal Learning tests.

2.3 | MRI acquisition

Participants were scanned with one of two very similar imaging protocols on the same 3T Siemens Prisma with a 64-channel head coil. Both protocols used the same T1-weighted sagittal magnetization prepared rapid acquisition gradient echo (MPRAGE) with TR/TE/TI 1,800/ 2.37/900 ms, $0.87 \times 0.87 \times 0.85$ mm^3, 208 slices, FOV 250×250 mm^2 in 3:39 min. For R2* and QSM, both protocols used an axial-oblique 3D multiple gradient echo sequence with TE1 3.82 ms, echo spacing 5.49 ms, FOV 240×202 mm^2, in-plane resolution of 0.94×0.94 mm^2, 260 Hz/pixel bandwidth and $2\times$ parallel imaging. There were slight variations in other parameters between the two cohorts: cohort 1 (n = 333 after exclusions; 5–90 years; 195 females) with 6 echoes, TR 37 ms, flip angle 13°, 1.7 mm slice thickness, 88 slices in 5:30 min and cohort 2 (n = 165 after exclusions; 5–74 years; 91 females) with 7 echoes, TR 45 ms, flip angle 17°, 2.0 mm slice thickness, and 64 slices with 6/8 slice partial Fourier in 3:40 min. Slight differences between protocols were mitigated by matching image resolution and echo number (described below). In addition, the effect of 6/8 slice partial Fourier was tested in a small number of subjects who were scanned with both protocols, yielding no significant differences in parameter values (p = .426, data not shown).

2.4 | Image processing

Susceptibility and R2* maps were computed from the multiple gradient-echo data. To harmonize the two cohorts, the thinner 1.7 mm slice thickness of cohort 1 was downsampled to 2.0 mm to match cohort 2, and both cohorts used only 6 echoes. R2* maps were

produced using mono-exponential fitting of magnitude signal at different echo-times (Du, Jin, Hu, & Tanabe, 2009). For QSM, phase from different echo-times were corrected for RF-related offsets, and spatially unwrapped using a best-path algorithm (Abdul-Rahman et al., 2007), and then fitted into a magnetic field map using magnitude-weighted least squares. A brain mask was generated using Brain Extraction Tool (BET) in FSL (Smith, 2002). Magnetic field contributions from sources outside of the brain were removed using Sophisticated Harmonic Artifact Removal for Phase data with variable kernel radii (V-SHARP) ranging from the minimum voxel dimension to a maximum of 9 mm (Li, Wu, & Liu, 2011; Schweser, Deistung, Lehr, & Reichenbach, 2011). The remnant local field was then inverted into a susceptibility map using nonlinear Morphology-Enabled Dipole Inversion (MEDI) algorithm with default settings, except a regularization parameter of 2,500 (Liu et al., 2013). Susceptibility values are not absolute and are typically normalized to another tissue or CSF (Feng et al., 2018; Straub et al., 2017). Nevertheless, this normalization is subject to error if using CSF, and can complicate interpretation if using another tissue given that both measures change independently over the lifespan. Reconstructed susceptibility maps are implicitly normalized to the mean value of the whole brain. Previous studies suggested using susceptibility values directly and showed no systematic bias between no normalization and normalization to either a white matter or CSF reference (Acosta-Cabronero et al., 2016; Li et al., 2014). For these reasons, susceptibility was not further normalized.

To rule out subjects with significant motion artifact, data quality for R2* and QSM was assessed by examining the multiple gradient echo sequence using an automated tool which was followed up with manual inspection of cases above a set artifact threshold. The automatic procedure used a background (i.e., air) region on the first echo magnitude images (Mortamet et al., 2009), which included all pixels outside the head mask superior to the nasion-to-posterior-of-the-cerebellum plane. Artifacts in the background region were then segmented based on an intensity histogram and quantified using the ratio of the number of artifact voxels to the total number of background voxels, with lower ratios implying better quality (Mortamet et al., 2009). Based on manual inspection of a subset of data from these protocols, a ratio of 0.17 in the automated QA was chosen as the threshold to flag data for subsequent manual inspection.

T1-weighted images were uploaded to volBrain (Manjón & Coupé, 2016) for segmentation to yield volumes (cm^3) and 3D regions of interest (ROIs) of bilateral thalamus, caudate, putamen and globus pallidus. ROI masks of the caudate, putamen and thalamus were then eroded by 1 voxel to avoid inclusions of surrounding tissues and minimize partial volume effects. R2*/QSM maps were rigidly co-registered to T1 images using ANTs (Avants et al., 2011) to yield R2* and QSM measurements for each structure using the T1-generated 3D ROIs.

2.5 | Volume, R2* and QSM versus age

Non-linear relationships between volume, R2* and QSM versus age were tested for each structure using the Curve Estimation Toolbox in

SPSS 26.0 (IBM Corp, Armork, New York). Quadratic, Cubic, and Exponential functions were tested, and adjusted R^2 values were compared between significant fits for each structure/measure. Curve fitting was initially performed separately in males and females with left and right separate, and then repeated twice for R2*/QSM: once with left/right structures averaged (but males and females separated) and then again with both left/right structures averaged and males and females combined. Residuals of the final best fit for each structure (left/right averaged and males/females combined) were used for correlations with cognitive testing.

2.6 | Hemispheric asymmetry and sex differences

Hemispheric asymmetry was tested via Z tests of corresponding curve fitting parameters (i.e., β(age), β(age^2), β(age^3), and β(constant) for cubic curves) in the left versus right counterparts of each structure/variable, separately in males and females. Likewise, sex differences were assessed via Z tests of corresponding fit parameters in males versus females (after combining left and right hemispheres). The p values were FDR corrected for multiple comparisons.

2.7 | Relationships between R2* and QSM

To assess differences between cross-sectional trajectories of R2* and QSM, the raw values of each variable were transformed to Z scores such that they could be plotted on the same scale (left/right and males/females combined). Best fit curves were applied to each, allowing both visual comparison of R2* versus QSM curves as well as Z tests of the β parameter values for each curve. In addition, to allow visualization of differences between R2* and QSM independent of curve fitting, a moving average with a 20-subject window was

calculated for Z scores for each parameter across the entire sample, shifted by one subject each average (i.e., the mean and SD for subjects 1–20, 2–21, 3–22, and so on, with subjects ordered by age).

2.8 | Correlations with cognitive scores

Relationships between cognitive performance and R2*/QSM values of each structure were assessed with Pearson's correlations between the residuals of each R2*/QSM lifespan curve (males/females and left/right combined) versus standard scores for Picture Sequence Memory Task, Dimensional Card Sorting and List Sorting Working Memory, or age corrected residuals for Rey Auditory Verbal Learning, and Oral Symbol Digit Task. The p values were FDR corrected for multiple comparisons.

3 | RESULTS

3.1 | Relationships with age

Caudate, putamen, globus pallidus, and thalamus volumes best fit exponential functions which indicated decreases with age across the 5–90 year old "lifespan" (Figure 1a). Conversely, R2* and susceptibility of all structures best fit cubic functions which suggested increases with age across the lifespan for the caudate, putamen, and globus pallidus, but an increase in childhood, plateau in mid-adulthood and decrease thereafter for both R2* and susceptibility of the thalamus (all $p < .001$, Figures 1 and 2, Table 1). R2* and susceptibility curves of the caudate, putamen and globus pallidus reached their highest value over 85 years of age. Likewise, 90% of total change in both R2* and susceptibility was reached in the later portions of the lifespan (65–87 years) for these structures, suggesting continual increase,
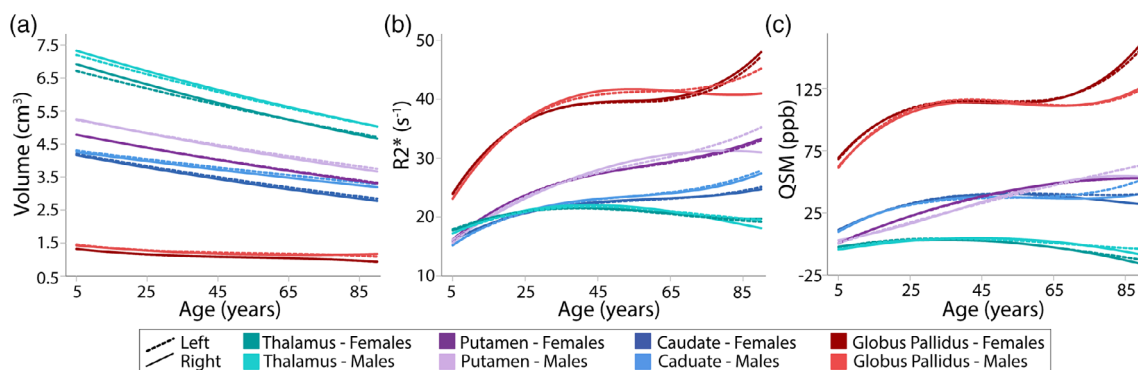
FIGURE 1 Best-fit curves across 5–90 year lifespan in 286 females and 212 males for (a) volume, (b) R2*, and (c) QSM of the thalamus, putamen, caudate and globus pallidus, separated by sex (different shade of each color) and hemisphere (solid vs. dashed lines). Volume decreased with age in all four structures, while R2* and QSM followed either quadratic or cubic curves that increased across the lifespan for all structures except the thalamus, which increased, reached a peak and then declined. R2* and QSM were highest in the globus pallidus across all ages. R2* and QSM in the other three structures were similar to each other at the youngest ages, but progressively deviated with increasing age, particularly after 45–50 years. Curves within each structure were remarkably similar between males and females as well as between the left and right hemispheres

FIGURE 2 Raw data (left and right hemispheres averaged; males and females colored separately) and best fit curves for R2* and QSM of the caudate, putamen, thalamus, and globus pallidus. VolBrain ROIs of the caudate (yellow), putamen (pink), globus pallidus (green), and thalamus (teal) are overlaid on (a) R2* and (b) QSM of a 53 year old female. (c–j) R2* and QSM showed robust nonlinear changes with age with large overlap between males and females. Both R2* and susceptibility of the putamen and globus pallidus increased over the lifespan, following similar trajectories. For the caudate, R2* increased across the lifespan while susceptibility increased until mid-adulthood and plateaued thereafter, increasing very little for the remainder of the lifespan. The thalamus was the only structure shown to increase in childhood, reach a peak in adulthood and decline thereafter for both measures
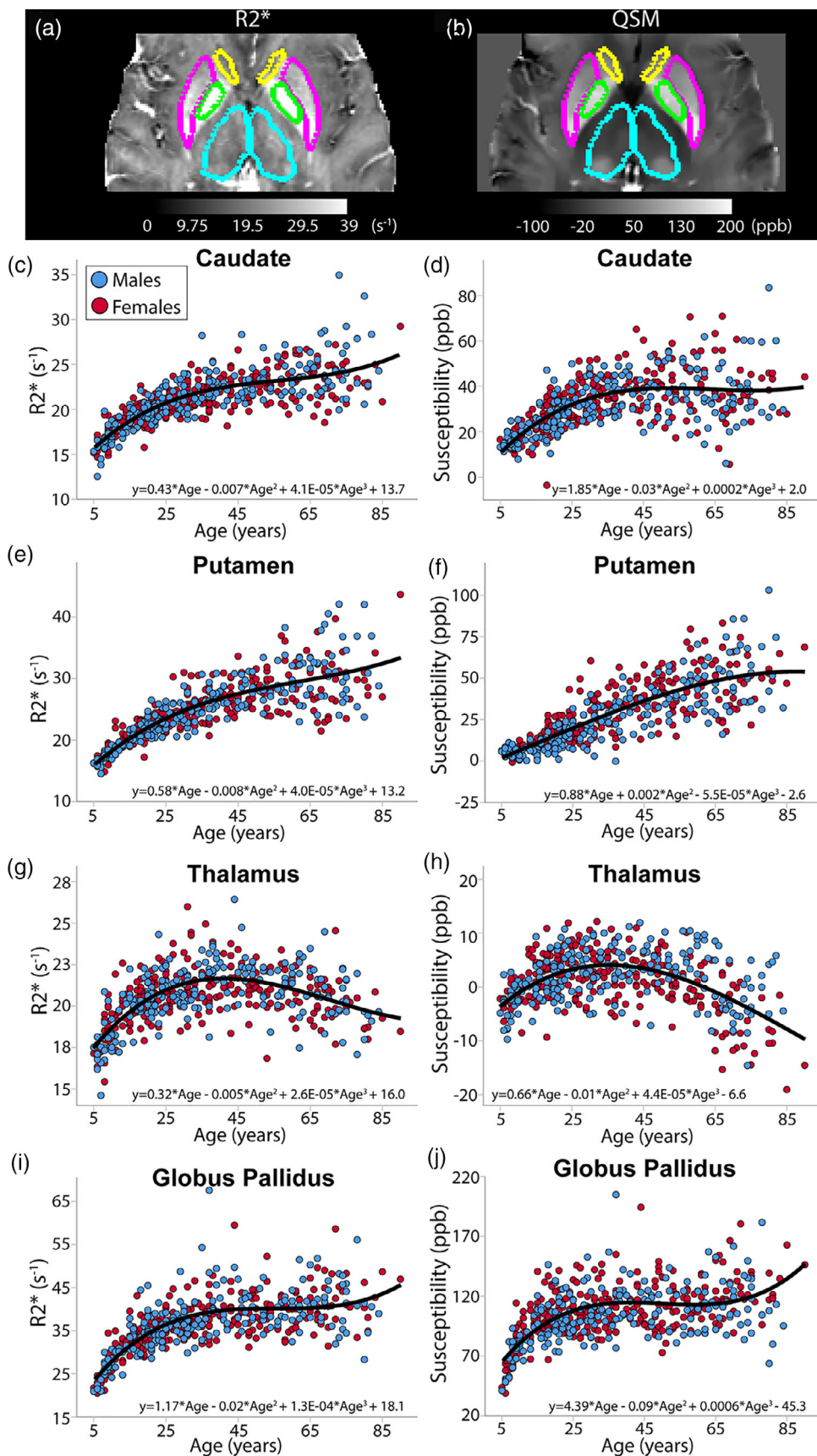
TABLE 1 Raw values predicted by curve fits for R2* and QSM

	Value at 5 years	Value at 90 years	Age at highest value	Age at 90% of total change from 5 to 90 years
Caudate				
R2*	16 s^{-1}	26 s^{-1}	>90 years	83 years
QSM	11 ppb	40 ppb	>90 years	36 years
Putamen				
R2*	16 s^{-1}	33 s^{-1}	>90 years	78 years
QSM	2 ppb	54 ppb	87 years	65 years
Thalamus				
R2*	18 s^{-1}	19 s^{-1}	41 years	n/a
QSM	−4 ppb	−9 ppb	36 years	n/a
Globus pallidus				
R2*	24 s^{-1}	46 s^{-1}	>90 years	85 years
QSM	65 ppb	147 ppb	>90 years	87 years

except for susceptibility of the caudate which reached 90% of total change at 36 years old followed by a leveling off at older ages (Table 1; Figure 2).

Unlike the continual increases observed in the basal ganglia, R2* and QSM curves of the thalamus reached peaks at 41 and 36 years, respectively, decreasing thereafter. R2* of the thalamus increased more than it decreased while the opposite was observed for susceptibility, which increased in childhood less than it decreased in later adulthood (Figure 2g,h).

As a post-hoc analysis an index of subject motion extracted from the automated QA procedure was added to cubic models and was not found to be significant for R2* or QSM of any structure (data not shown), suggesting that age related changes are not accounted for by subject motion.

3.2 | Hemispheric asymmetry

Nearly identical curve fits were observed for volumes, R2* and QSM of the left and right counterpart of each structure (Figure 1). Z tests of the left and right counterparts of each structure yielded no significant differences in the constant or age parameters for any measure. Thus, left and right sides were combined for all measures.

3.3 | Sex differences

Males and females were best fit to the same function versus age for all measures (Figure 1) except volume of the globus pallidus, which was best fit to a cubic function in females and a quadratic function in males. Z tests of corresponding β parameters in males versus females yielded no significant differences for any QSM or R2* fits. Conversely, there were three significant volume differences: the age parameter of the caudate (steeper decrease in females; corrected $p = .028$) as well as the constant of the putamen (larger volume in males; corrected

$p < .001$) and thalamus (larger volume in males; corrected $p = .002$). Given the minimal sex differences (including none in the variables of interest: QSM or R2*) and large degree of overlap in the raw data shown separately for males and females (Figure 2), subsequent analysis was carried out with males and females combined.

3.4 | Qualitative evaluation of regional change on the QSM and R2* maps

Examination of the R2* and QSM maps over the lifespan showed visible differences within the deep gray matter with age, particularly between very young children and adolescents/young adults as well as in older subjects (Figure 3). A sharp increase of both R2* and QSM can be seen in the globus pallidus from 5 to 15 years of age, in keeping with the curves reported above in the quantitative analysis. However, there also appears to be an anterior-to-posterior gradient of susceptibility change with the anterior portion of the globus pallidus increasing first at the youngest ages, which is only appreciated by examining the maps (Figures 3 and 4).

R2* contrast between the caudate and putamen became visible between 5 and 15 years of age, in keeping with quantitative parameter curves for these structures which start out with similar values at age 5, diverging with age. This contrast disappeared in later adulthood (75–85 years of age; Figure 3); however, the high iron content of both structures impedes visual distinction. Likewise, susceptibility contrast between the caudate and putamen is also evident in very young subjects (Figure 4), becoming less apparent around approximately 80 years of age (Figure 5).

Curve fitting suggests that QSM and R2* values in the thalamus increased slowly over 5–25 years, accompanied by less visible change in parameter maps than other structures. However, the susceptibility of the pulvinar (posterior nuclei of the thalamus) became substantially more visible between 15 and 25 years, again indicating regional heterogeneity that is not appreciated by QSM measurements of the whole structure (Figures 3 and 4). Susceptibility of the pulvinar remained elevated relative to the rest of the thalamus in most subjects in later adulthood (Figure 5).

FIGURE 3 Examples of T1-weighted MPRAGE, R2*, and QSM susceptibility maps from one subject per decade across the lifespan. T1 contrast is similar across subjects while both R2* and QSM change visibly within the first two decades continuing until the 90s. Although R2* changes visibly across the lifespan, QSM appears to provide more contrast between structures (e.g., putamen vs. globus pallidus, which are less distinguishable on R2* by 90 years of age), as well as heterogeneity within structures, for example, the pulvinar of the thalamus (posterior bright region on QSM)
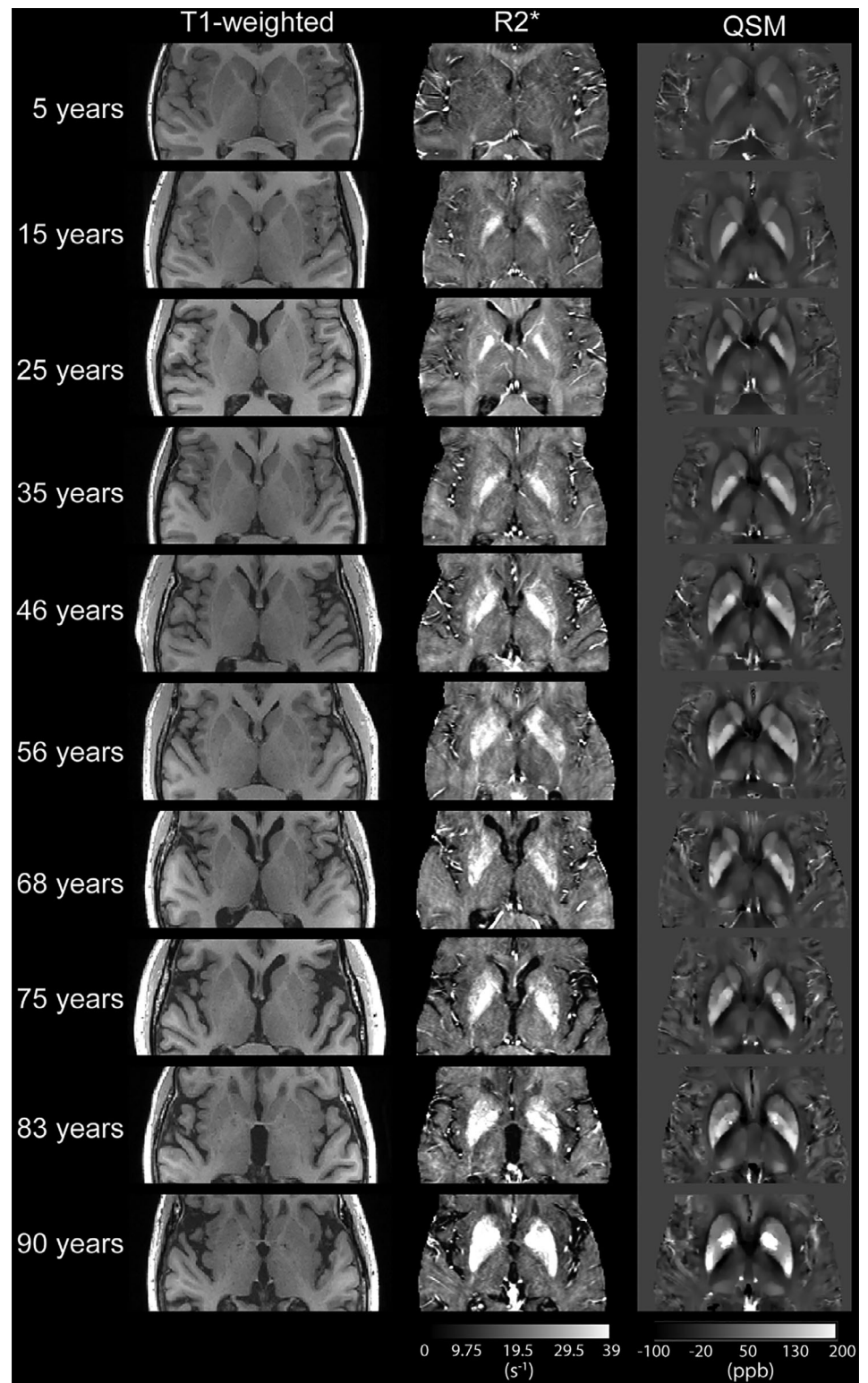

3.5 | Relationships between R2* and QSM

Curve fits of R2* and QSM Z scores, plotted on the same scale, suggest a great degree of overall similarity in the patterns of change with age between these two parameters (Figure 6a,c,e,g). Both the caudate (Figure 6a) and globus pallidus (Figure 6g) show nearly perfect overlap from 5 to approximately 35 years of age, after which the curves diverge slightly for the globus pallidus and more substantially for the caudate (with continued increases in R2*). However, the β parameters of these fits were not significantly different (R2* vs. QSM) for either structure, likely resulting from the large increase in variance seen at older age for both parameters (Figure 6b,h; Table 2). Conversely,
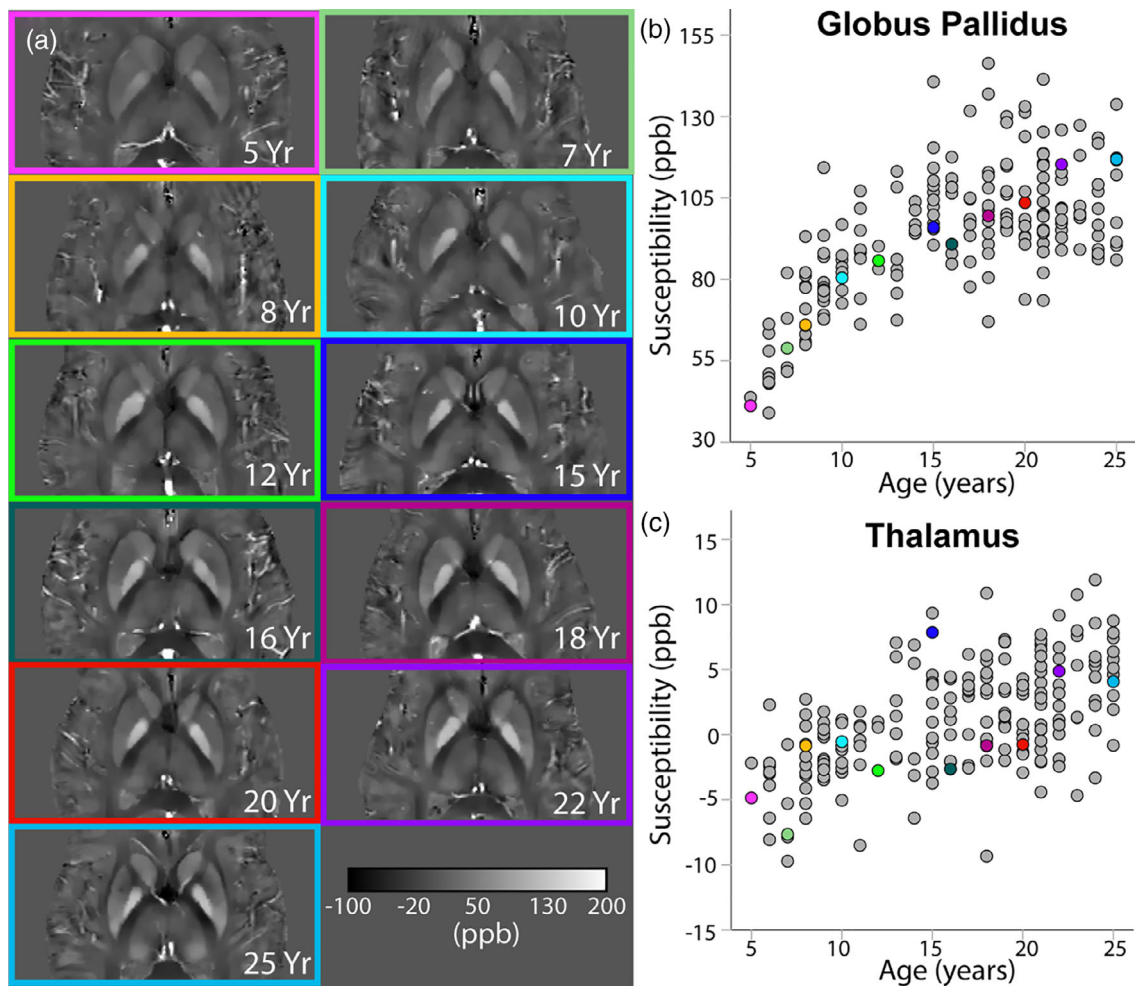
FIGURE 4 (a) Susceptibility maps from childhood to early adulthood for example subjects ranging from 5 to 25 years old, along with plots for (b) globus pallidus and (c) thalamus with example subjects from (a) identified by colored dots. In the globus pallidus, susceptibility increased rapidly within the 5–10 years range, evident both visually in the first four subjects as well as in the plots. In addition, there appears to be an anterior-to-posterior gradient with the anterior portion increasing first as only appreciated by examining the maps. Conversely, susceptibility in the thalamus increased slowly over 5–25 years, with much less visible change overall. However, the pulvinar (posterior nucleus of the thalamus) susceptibility is shown to increase substantially between 20 and 25 years on the actual susceptibility maps which indicates regional heterogeneity that is not appreciated by whole structure measurements
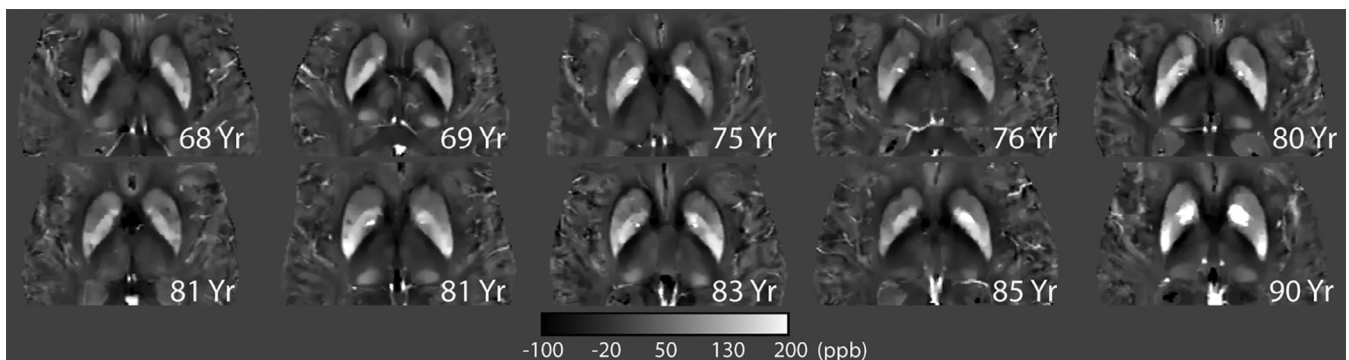
FIGURE 5 Susceptibility maps from 10 females aged 68–90 years, showing substantially elevated values in the globus pallidus relative to the other three deep gray matter regions, as well as the in the pulvinar relative to the rest of the thalamus. However, in these older females there is also marked inter-subject variability in both structures (e.g., globus pallidus susceptibility much higher in the 75 year old versus 76 year old, pulvinar not visible in the 75 year old; barely visible in the first 81 year old or 85 year old, yet very clear in most other subjects). In addition, the ability to visually distinguish the caudate from the putamen appears to be lost around approximately 80 years of age

FIGURE 6 R2* and QSM values converted to Z scores to permit comparison on the same scale. The left column (a,c,e,g) show curve fits for structure, with arrows indicating statistically significant differences in parameter values between R2* and QSM. The right column (b,d,f,h) show ±1SD of the moving average of each measure (average of 20 consecutive subjects, window shifted every 1 subject). R2* and QSM curves overlaped substantially, with a few notable exceptions (e.g., the thalamus). Moving average curves provide additional visualization of the overlap between R2* and QSM curves (overlap shown in purple), while also highlighting places where the curves differ, for example, youngest ages in the putamen. Furthermore, in all structures the SD of both Z scores increased with age, particularly for the caudate, putamen, and globus pallidus
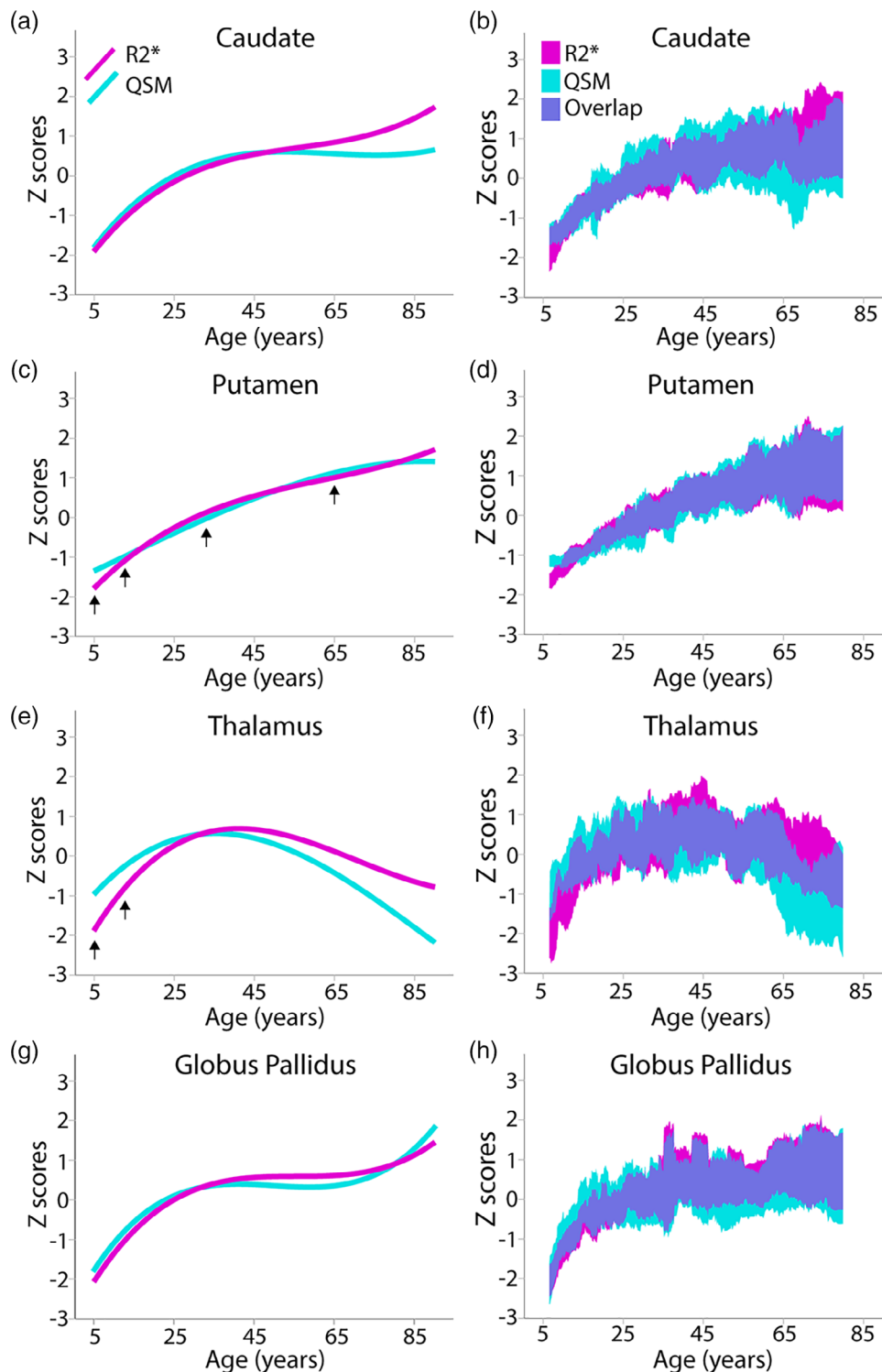
curve fits of putamen R2* and QSM yielded subtle but significant differences in all β parameters (constant, age, age^2, and age^3; Figure 6c). These subtle differences are also evident in the moving averages (not constrained by fitting parameters; Figure 6d), which show extremely tight standard deviations and no overlap between the putamen Z scores of QSM and R2* at the youngest ages below 9 years. The first inflection (age^2 parameter) for R2* and QSM of the putamen is opposite in direction (Table 2), which can again be appreciated when

looking at the moving averages of subjects from approximately 10 to 25 years of age (Figure 6d). Similar to the caudate and globus pallidus, an increase in variance is seen for both R2* and QSM of the putamen in older subjects (Figure 6d). Lastly, Z tests of the β parameters of thalamus curve fits indicate significant differences in both the constant and age parameters, with R2* starting lower and increasing more steeply than QSM, while the opposite pattern is observed from the peak to oldest ages (Figure 6e). Although an increase in inter-subject

	Adjusted R^2	β (constant)	β (age)	β (age^2)	β (age^3)
Caudate					
R2*	0.634	−2.58	0.15	−2.4E-3	1.4E-5
QSM	0.433	−2.51	0.15	−2.5E-3	1.3E-5
Putamen					
R2*	0.712	−2.32	0.12	−1.5E-3	8.0E-6
QSM	0.671	−1.58	0.05	1.2E-4	−3.0E-06
Thalamus					
R2*	0.401	−2.76	0.20	−3.3E-3	1.6E-5
QSM	0.285	−1.56	0.13	−2.3E-3	9.0E-6
Globus pallidus					
R2*	0.550	−2.91	0.19	−3.4E-3	2.0E-5
QSM	0.351	−2.67	0.19	−4.0E-3	2.7E-5

TABLE 2 Beta parameter values for curve fits of R2* and QSM Z scores (for comparison on the same scale)

variability is again observed in older subjects (Figure 6f), this change is much less striking than for the other deep gray matter structures.

3.6 | Correlations with cognition

Means and standard deviations of age-corrected standard scores for the Picture Sequence Memory, Dimensional Card Sorting, and List Sorting Working Memory tasks were 111 ± 17, 111 ± 17, and 103 ± 14, respectively, indicating average to high-average performance in this sample. The NIH Toolbox does not yield standard scores for Auditory Verbal Learning and Oral Symbol Digit tasks. Raw scores for these measures were 27 ± 6 and 90 ± 20, respectively. Picture Sequence Memory and Oral Symbol Digit scores were positively correlated with caudate susceptibility ($R = 0.123$, $p = .007$ and $R = 0.109$, $p = .021$, respectively), while Picture Sequence Memory scores were also positively correlated with putamen susceptibility ($R = 0.101$, $p = .026$); however, these correlations did not survive FDR correction.

4 | DISCUSSION

This study demonstrates cross-sectional trajectories of R2* and QSM indicative of putative changes in brain iron in the caudate, putamen, globus pallidus and thalamus from 5 to 90 years of age in a large cohort of 498 healthy subjects. Trajectories were strikingly similar between hemispheres and sex, suggesting robust relationships with age given that males and females were fit independently. This work confirms previous findings and adds to the currently limited literature examining putative iron changes in deep gray matter from samples that span both childhood and adulthood (Aquino et al., 2009: 1–80 years, $n = 80$; Li et al., 2014: 1–81 years, $n = 191$; Zhang et al., 2018: 1–81 years, $n = 191$), only one of which included both R2* and QSM (Li et al., 2014).

4.1 | Age related increase of R2* and QSM in the basal ganglia continue across the lifespan

Increases of R2* and QSM with age continued across the lifespan in the globus pallidus, caudate and putamen, albeit at rates that varied by structure. Both R2* and QSM reached 90% of total change during the mid-60s to late-80s reflecting continued steady increases into late adulthood, with the notable exception of susceptibility of the caudate which reached 90% of total change in the late 30s, increasing only gradually thereafter. Previous studies including subjects across the lifespan also found steep changes with age in the globus pallidus during childhood that subsequently leveled off in adulthood, and shallower but more protracted curves for the caudate and putamen (Aquino et al., 2009; Li et al., 2014). Likewise, the globus pallidus has been shown to have the steepest slope of change with age relative to other structures in early development (Ning et al., 2019), and minimal (Persson et al., 2015) or no significant change with age during adulthood (Acosta-Cabronero et al., 2016; Li et al., 2020). Although the majority of change observed in the globus pallidus in this study occurred in childhood, we also observe a late life increase of R2* and QSM that is not consistent with other studies. This increase may be an artifact of curve fitting as moving average data suggests a steady continued increase, but may also result from elevated inter-subject variability observed at these older age (discussed further below).

4.2 | The thalamus follows a distinct age trajectory relative to the basal ganglia

Both R2* and QSM of the thalamus followed a distinct pattern relative to the other three deep gray matter structures, increasing until the late 30s to early 40s and then decreasing thereafter for the remainder of the lifespan in keeping with previous autopsy work indicating a peak of iron in the thalamus at 35 years of age (Hallgren & Sourander, 1958). This finding is also in agreement with previous

QSM work indicating an increase followed by a decrease in the whole thalamus (Zhang et al., 2018). However, Zhang et al. (2018) further show distinct patterns within thalamic nuclei, including an increase of susceptibility in the pulvinar that reaches a plateau that does not then decrease (Zhang et al., 2018), which was also qualitatively observed here (though not measured). The propensity for the basal ganglia to continue to accumulate iron while the thalamus loses iron after mid-life has been speculated to relate to the role of these structures in motor versus sensory functions, respectively (Acosta-Cabronero et al., 2016) or differential susceptibility to dysregulation of iron metabolism (Ward et al., 2014). However, this unique pattern may also reflect changes to myelin. Although both the globus pallidus and thalamus are high in myelin relative to the caudate and putamen, the globus pallidus is also very high in iron, overshadowing the effects of myelin on its R2* and QSM trajectories. Conversely, the thalamus is high in myelin (concentrated within the internal and external inter-medullary lamina) but low in iron, which could amplify the relatively minor contribution of myelin to susceptibility signal. Change with age from 5 years to young adulthood was steeper for R2* than for suscep-tibility, which is likely due to the additive effects of myelination on R2* in the thalamus. Conversely, the slope of susceptibility loss after the mid-30s to 40s was steeper than for R2*, suggesting that QSM may be more sensitive to non-heme iron loss known to occur over this age range in the thalamus (Hallgren & Sourander, 1958), also given that myelin loss in the thalamus would attenuate this QSM decrease rather than accelerate it (Liu, Li, Johnson, & Wu, 2011).

4.3 | Regional heterogeneity is observed within deep gray matter regions

Whole-structure quantitative measures were complemented by qual-itative evaluation of parameter maps, which indicated regional het-erogeneity within structures, such as increasing susceptibility in the pulvinar at older ages (despite whole-structure decreases of the thalamus after mid-life). Likewise, an anterior to posterior gradient of susceptibility increase with age was observed in the globus pallidus among young children, as well as increasing susceptibility in the posterior putamen among older subjects, neither of which are appreciable by examination of the whole structures. Keuken et al. (2017) also show greater susceptibility in posterior putamen in middle-aged and elderly subjects but not young adults. Further examination of the subregions that comprise these structures is needed.

4.4 | Patterns of volume change are distinct from R2* and QSM

R2* and QSM followed distinct patterns of change with age relative to volume, which decreased at a relatively even pace across the lifespan. Nonetheless, to determine if volume atrophy contributed to elevations of R2* and QSM, a post-hoc analysis was conducted adding intracranial volume and structure volume to cubic models of R2* and QSM versus age. Structure volume was significant in the models of thalamus and putamen QSM versus age ($p = .039$ and $p < .001$, respectively). Likewise, intracranial volume was significant in the model of thalamus R2* versus age ($p = .027$). However, adding vol-umes to these models only explained an additional 0.6–2.5% of the variance. This suggests that age related changes in R2* and QSM are largely independent of changes in brain volumes, in keeping with past work demonstrating no correlation between R2*/QSM and volume ($n = 30$, 20–41 years; Péran et al., 2009).

4.5 | The relationship between R2* and QSM is complementary

Although the overall pattern of change between QSM and R2* is remarkably similar, comparison on the same scale (via conversion to Z scores) enabled comparison of the age-related differences in the relationship between these measures. From early childhood to the late teens, Z score curves of R2* increased more rapidly than sus-ceptibility of both the putamen and thalamus (Figure 6c,e), presum-ably due to the additive effects of iron accumulation and myelination, while myelin is subtractive for QSM. In the caudate, continued steep increases of R2* relative to QSM in older subjects may relate to increasing microcalcification (Betts et al., 2016) that would reduce susceptibility while increasing R2*; however, this divergence of the Z scores curves in later adulthood was not statistically significant. Age related changes in the relationship between R2* and QSM cannot be appreciated by measuring correlations pooled across ages and struc-tures, as done in past literature (e.g., Betts et al., 2016; Li et al., 2014; Peterson et al., 2019).

4.6 | Inter-subject variability increases with age

The raw data in Figure 2 as well as the moving-average standard devi-ations shown in Figure 6 indicate that inter-subject variability of R2* and QSM increased with age across the lifespan. Indeed, the range of R2* values in the caudate and putamen in the last two decades of the lifespan were nearly double that of the first two decades. This vari-ability can be also appreciated visually, for example, inconsistent visi-bility of the pulvinar is apparent among older subjects (Figure 5) relative to younger subjects (Figure 4). An increase in variability with age is also apparent in Hallgren and Sourander (1958), as well as in the raw QSM and R2* plots of Li et al. (2014), suggesting this may be a consistent finding. Increased variability among elderly subjects rela-tive to children and adolescents may reflect an accumulation of life-style and other factors (e.g., cardiovascular disease, smoking, and body mass index) shown to influence measures of brain aging includ-ing iron deposition, brain volumes, and white mater hyperintensities (Debette et al., 2011; Pirpamer et al., 2016). These additional factors were not measured here and may account for some of the variability observed among older subjects.

4.7 | Limitations

Several nonbiological factors must be considered when comparing relationships with age as well as when comparing to previous literature. By definition, the choice of statistical fitting parameters impacts resulting trajectories (particularly in cross-sectional datasets), and also complicates comparison between studies. One of the other QSM lifespan studies (Li et al., 2014), as well as the formative autopsy study examining iron content (Hallgren & Sourander, 1958) exclusively used exponential growth models on all structures (except the thalamus) without comparison to other models. As a post-hoc analysis, the exponential growth model was plotted against the best fit model chosen here (data not shown). The exponential growth curve yields a similar approximation of the data in the first half of the lifespan for most structures, closely matching the steep upswing seen in the moving average during early childhood, but is unable to model the continued increases in later adulthood, underscoring the challenge of curve fitting in lifespan data. Sample characteristics such as age range and distribution of cross-sectional data vary widely across the R2*/QSM literature, and are known to influence some statistical fits more than others (Fjell et al., 2010). To overcome these limitations moving average data was also presented here, which is free from fitting constraints. The present study offers a further advantage over previous literature by the inclusion of a greater number of subjects in middle ages of the lifespan which may mitigate extrapolation between young and older subjects. Although this study includes subjects as young as 5 years of age, this excludes critical years of early development marked by large changes in tissue susceptibility (Ning et al., 2019; Zhang et al., 2019) and iron accumulation (Hallgren & Sourander, 1958). Future work should strive to include large longitudinal cohorts spanning all ages to confirm cross-sectional findings.

5 | CONCLUSIONS

This cross-sectional study confirms past work documenting nonlinear and regionally dependent changes of putative brain iron in deep gray matter across the lifespan, which are not accounted for by changes in structure volume. The large sample size is sufficient to confirm a lack of sex or hemispheric differences, in keeping with other smaller studies. Inter-subject variability is shown to increase substantially at older ages for both R2* and QSM, potentially reflecting the influence of genetic, environmental and lifestyle factors that accumulate over time. This work provides a baseline for studies examining the role of myelin and brain iron in neurodevelopmental and neurodegenerative disorders.

ORCID

Sarah Treit https://orcid.org/0000-0002-6040-6016

REFERENCES

Abdul-Rahman, H. S., Gdeisat, M. A., Burton, D. R., Lalor, M. J., Lilley, F., & Moore, C. J. (2007). Fast and robust three-dimensional best path phase unwrapping algorithm. *Applied Optics*, *46*, 6623–6635.

Acosta-Cabronero, J., Betts, M. J., Cardenas-Blanco, A., Yang, S., & Nestor, P. J. (2016). In vivo MRI mapping of brain iron deposition across the adult lifespan. *The Journal of Neuroscience: The Official Journal of the Society for Neuroscience*, *36*, 364–374.

Aquino, D., Bizzi, A., Grisoli, M., Garavaglia, B., Bruzzone, M. G., Nardocci, N., … Chiapparini, L. (2009). Age-related iron deposition in the basal ganglia: Quantitative analysis in healthy subjects. *Radiology*, *252*, 165–172.

Avants, B. B., Tustison, N. J., Song, G., Cook, P. A., Klein, A., & Gee, J. C. (2011). A reproducible evaluation of ANTs similarity metric performance in brain image registration. *NeuroImage*, *54*, 2033–2044.

Beard, J. (2003). Iron deficiency alters brain development and functioning. *Journal of Nutrition*, *133*, 1468s–1472s.

Betts, M. J., Acosta-Cabronero, J., Cardenas-Blanco, A., Nestor, P. J., & Düzel, E. (2016). High-resolution characterisation of the aging brain using simultaneous quantitative susceptibility mapping (QSM) and R2* measurements at 7T. *NeuroImage*, *138*, 43–63.

Bilgic, B., Pfefferbaum, A., Rohlfing, T., Sullivan, E. V., & Adalsteinsson, E. (2012). MRI estimates of brain iron concentration in normal aging using quantitative susceptibility mapping. *NeuroImage*, *59*, 2625–2635.

Carpenter, K. L. H., Li, W., Wei, H., Wu, B., Xiao, X., Liu, C., … Egger, H. L. (2016). Magnetic susceptibility of brain iron is associated with childhood spatial IQ. *NeuroImage*, *132*, 167–174.

Cortese, S., Azoulay, R., Castellanos, F. X., Chalard, F., Lecendreux, M., Chechin, D., … Konofal, E. (2012). Brain iron levels in attention-deficit/hyperactivity disorder: A pilot MRI study. *The World Journal of Biological Psychiatry*, *13*, 223–231.

Darki, F., Nemmi, F., Möller, A., Sitnikov, R., & Klingberg, T. (2016). Quantitative susceptibility mapping of striatum in children and adults, and its association with working memory performance. *NeuroImage*, *136*, 208–214.

Daugherty, A. M., & Raz, N. (2016). Accumulation of iron in the putamen predicts its shrinkage in healthy older adults: A multi-occasion longitudinal study. *NeuroImage*, *128*, 11–20.

Daugherty, A. M., Hoagey, D. A., Kennedy, K. M., & Rodrigue, K. M. (2019). Genetic predisposition for inflammation exacerbates effects of striatal iron content on cognitive switching ability in healthy aging. *NeuroImage*, *185*, 471–478.

Debette, S., Seshadri, S., Beiser, A., Au, R., Himali, J. J., Palumbo, C., … DeCarli, C. (2011). Midlife vascular risk factor exposure accelerates structural brain aging and cognitive decline. *Neurology*, *77*, 461–468.

Du, Y. P., Jin, Z., Hu, Y., & Tanabe, J. (2009). Multi-echo acquisition of MR angiography and venography of the brain at 3 tesla. *Journal of Magnetic Resonance Imaging: JMRI*, *30*, 449–454.

Farrall, A. J., & Wardlaw, J. M. (2009). Blood-brain barrier: Ageing and microvascular disease–systematic review and meta-analysis. *Neurobiology of Aging*, *30*, 337–352.

Feng, X., Deistung, A., & Reichenbach, J. R. (2018). Quantitative susceptibility mapping (QSM) and R(2)(*) in the human brain at 3T: Evaluation of intra-scanner repeatability. *Zeitschrift für Medizinische Physik, 28*, 36–48.

Fillebeen, C., Descamps, L., Dehouck, M. P., Fenart, L., Benaïssa, M., Spik, G., ... Pierce, A. (1999). Receptor-mediated transcytosis of lactoferrin through the blood-brain barrier. *The Journal of Biological Chemistry, 274*, 7011–7017.

Fjell, A. M., Walhovd, K. B., Westlye, L. T., Ostby, Y., Tamnes, C. K., Jernigan, T. L., ... Dale, A. M. (2010). When does brain aging accelerate? Dangers of quadratic fits in cross-sectional studies. *NeuroImage, 50*, 1376–1383.

Gershon, R. C., Cella, D., Fox, N. A., Havlik, R. J., Hendrie, H. C., & Wagster, M. V. (2010). Assessment of neurological and behavioural function: The NIH toolbox. *The Lancet Neurology, 9*, 138–139.

Ghadery, C., Pirpamer, L., Hofer, E., Langkammer, C., Petrovic, K., Loitfelder, M., ... Schmidt, R. (2015). R2* mapping for brain iron: Associations with cognition in normal aging. *Neurobiology of Aging, 36*, 925–932.

Gong, N. J., Wong, C. S., Hui, E. S., Chan, C. C., & Leung, L. M. (2015). Hemisphere, gender and age-related effects on iron deposition in deep gray matter revealed by quantitative susceptibility mapping. *NMR in Biomedicine, 28*, 1267–1274.

Haacke, E. M., Cheng, N. Y., House, M. J., Liu, Q., Neelavalli, J., Ogg, R. J., ... Obenaus, A. (2005). Imaging iron stores in the brain using magnetic resonance imaging. *Magnetic Resonance Imaging, 23*, 1–25.

Haacke, E. M., Miao, Y., Liu, M., Habib, C. A., Katkuri, Y., Liu, T., ... Wu, J. (2010). Correlation of putative iron content as represented by changes in R2* and phase with age in deep gray matter of healthy adults. *Journal of Magnetic Resonance Imaging: JMRI, 32*, 561–576.

Hallgren, B., & Sourander, P. (1958). The effect of age on the non-Haemin iron in the human brain. *Journal of Neurochemistry, 3*, 41–51.

Hasegawa, M., Houdou, S., Mito, T., Takashima, S., Asanuma, K., & Ohno, T. (1992). Development of myelination in the human fetal and infant cerebrum: A myelin basic protein immunohistochemical study. *Brain and Development, 14*, 1–6.

Hect, J. L., Daugherty, A. M., Hermez, K. M., & Thomason, M. E. (2018). Developmental variation in regional brain iron and its relation to cognitive functions in childhood. *Developmental Cognitive Neuroscience, 34*, 18–26.

Keuken, M. C., Bazin, P. L., Backhouse, K., Beekhuizen, S., Himmer, L., Kandola, A., ... Forstmann, B. U. (2017). Effects of aging on T, T_2*, and QSM MRI values in the subcortex. *Brain Structure & Function, 222*, 2487–2505.

Langkammer, C., Krebs, N., Goessler, W., Scheurer, E., Ebner, F., Yen, K., ... Ropele, S. (2010). Quantitative MR imaging of brain iron: A postmortem validation study. *Radiology, 257*, 455–462.

Langkammer, C., Schweser, F., Krebs, N., Deistung, A., Goessler, W., Scheurer, E., ... Reichenbach, J. R. (2012). Quantitative susceptibility mapping (QSM) as a means to measure brain iron? A post mortem validation study. *NeuroImage, 62*, 1593–1599.

Larsen, B., Bourque, J., Moore, T. M., Adebimpe, A., Calkins, M. E., Elliott, M. A., ... Satterthwaite, T. D. (2020). Longitudinal development of brain iron is linked to cognition in youth. *The Journal of Neuroscience, 40*, 1810–1818.

Li, W., Wu, B., & Liu, C. (2011). Quantitative susceptibility mapping of human brain reflects spatial variation in tissue composition. *NeuroImage, 55*, 1645–1656.

Li, W., Wu, B., Batrachenko, A., Bancroft-Wu, V., Morey, R. A., Shashi, V., ... Liu, C. (2014). Differential developmental trajectories of magnetic susceptibility in human brain gray and white matter over the lifespan. *Human Brain Mapping, 35*, 2698–2713.

Li, Y., Sethi, S. K., Zhang, C., Miao, Y., Yerramsetty, K. K., Palutla, V. K., ... Haacke, E. M. (2020). Iron content in deep gray matter as a function of age using quantitative susceptibility mapping: A multicenter study. *Frontiers in Neuroscience, 14*, 607705.

Liu, C., Li, W., Johnson, G. A., & Wu, B. (2011). High-field (9.4 T) MRI of brain dysmyelination by quantitative mapping of magnetic susceptibility. *NeuroImage, 56*, 930–938.

Liu, T., Wisnieff, C., Lou, M., Chen, W., Spincemaille, P., & Wang, Y. (2013). Nonlinear formulation of the magnetic field to source relationship for robust quantitative susceptibility mapping. *Magnetic Resonance in Medicine, 69*, 467–476.

Lozoff, B., & Georgieff, M. K. (2006). Iron deficiency and brain development. *Seminars in Pediatric Neurology, 13*, 158–165.

Manjón, J. V., & Coupé, P. (2016). volBrain: An online MRI brain volumetry system. *Frontiers in Neuroinformatics, 10*, 30.

Mills, E., Dong, X. P., Wang, F., & Xu, H. (2010). Mechanisms of brain iron transport: Insight into neurodegeneration and CNS disorders. *Future Medicinal Chemistry, 2*, 51–64.

Moos, T., Rosengren Nielsen, T., Skjørringe, T., & Morgan, E. H. (2007). Iron trafficking inside the brain. *Journal of Neurochemistry, 103*, 1730–1740.

Mortamet, B., Bernstein, M. A., Jack, C. R., Jr., Gunter, J. L., Ward, C., Britson, P. J., ... Krueger, G. (2009). Automatic quality assessment in structural brain magnetic resonance imaging. *Magnetic Resonance in Medicine, 62*, 365–372.

Ning, N., Liu, C., Wu, P., Hu, Y., Zhang, W., Zhang, L., ... Jin, C. (2019). Spatiotemporal variations of magnetic susceptibility in the deep gray matter nuclei from 1 month to 6 years: A quantitative susceptibility mapping study. *Journal of Magnetic Resonance Imaging, 49*, 1600–1609.

Persson, N., Wu, J., Zhang, Q., Liu, T., Shen, J., Bao, R., ... Spincemaille, P. (2015). Age and sex related differences in subcortical brain iron concentrations among healthy adults. *NeuroImage, 122*, 385–398.

Peterson, E. T., Kwon, D., Luna, B., Larsen, B., Prouty, D., De Bellis, M. D., ... Pfefferbaum, A. (2019). Distribution of brain iron accrual in adolescence: Evidence from cross-sectional and longitudinal analysis. *Human Brain Mapping, 40*, 1480–1495.

Pirpamer, L., Hofer, E., Gesierich, B., De Guio, F., Freudenberger, P., Seiler, S., ... Schmidt, R. (2016). Determinants of iron accumulation in the normal aging brain. *Neurobiology of Aging, 43*, 149–155.

Péran, P., Cherubini, A., Luccichenti, G., Hagberg, G., Démonet, J. F., Rascol, O., ... Sabatini, U. (2009). Volume and iron content in basal ganglia and thalamus. *Human Brain Mapping, 30*, 2667–2675.

Ramos, P., Santos, A., Pinto, N. R., Mendes, R., Magalhães, T., & Almeida, A. (2014). Iron levels in the human brain: A post-mortem study of anatomical region differences and age-related changes. *Journal of Trace Elements in Medicine and Biology, 28*, 13–17.

Rouault, T. A. (2013). Iron metabolism in the CNS: Implications for neurodegenerative diseases. *Nature Reviews Neuroscience, 14*, 551–564.

Schenck, J. F., & Zimmerman, E. A. (2004). High-field magnetic resonance imaging of brain iron: Birth of a biomarker? *NMR in Biomedicine, 17*, 433–445.

Schweser, F., Deistung, A., Lehr, B. W., & Reichenbach, J. R. (2011). Quantitative imaging of intrinsic magnetic tissue properties using MRI signal phase: An approach to in vivo brain iron metabolism? *NeuroImage, 54*, 2789–2807.

Smith, S. M. (2002). Fast robust automated brain extraction. *Human Brain Mapping, 17*, 143–155.

Spincemaille, P., Liu, Z., Zhang, S., Kovanlikaya, I., Ippoliti, M., Makowski, M., ... Wang, Y. (2019). Clinical integration of automated processing for brain quantitative susceptibility mapping: Multi-site reproducibility and single-site robustness. *Journal of Neuroimaging, 29*, 689–698.

Straub, S., Schneider, T. M., Emmerich, J., Freitag, M. T., Ziener, C. H., Schlemmer, H. P., ... Laun, F. B. (2017). Suitable reference tissues for quantitative susceptibility mapping of the brain. *Magnetic Resonance in Medicine, 78*, 204–214.

Sun, H., Walsh, A. J., Lebel, R. M., Blevins, G., Catz, I., Lu, J. Q., … Wilman, A. H. (2015). Validation of quantitative susceptibility mapping with Perls' iron staining for subcortical gray matter. *NeuroImage*, *105*, 486–492.

Tang, S., Xu, Y., Liu, X., Chen, Z., Zhou, Y., Nie, L., & He, L. (2020). Quantitative susceptibility mapping shows lower brain iron content in children with autism. *European Radiology*, *31*, 2073–2083.

Tullo, S., Patel, R., Devenyi, G. A., Salaciak, A., Bedford, S. A., Farzin, S., … Chakravarty, M. M. (2019). MR-based age-related effects on the striatum, globus pallidus, and thalamus in healthy individuals across the adult lifespan. *Human Brain Mapping*, *40*, 5269–5288.

Wang, Y., & Liu, T. (2015). Quantitative susceptibility mapping (QSM): Decoding MRI data for a tissue magnetic biomarker. *Magnetic Resonance in Medicine*, *73*, 82–101.

Wang, Y., Spincemaille, P., Liu, Z., Dimov, A., Deh, K., Li, J., … Prince, M. R. (2017). Clinical quantitative susceptibility mapping (QSM): Biometal imaging and its emerging roles in patient care. *Journal of Magnetic Resonance Imaging: JMRI*, *46*, 951–971.

Ward, R. J., Zucca, F. A., Duyn, J. H., Crichton, R. R., & Zecca, L. (2014). The role of iron in brain ageing and neurodegenerative disorders. *The Lancet Neurology*, *13*, 1045–1060.

Zhang, Y., Wei, H., Cronin, M. J., He, N., Yan, F., & Liu, C. (2018). Longitudinal atlas for normative human brain development and aging over the lifespan using quantitative susceptibility mapping. *NeuroImage*, *171*, 176–189.

Zhang, Y., Shi, J., Wei, H., Han, V., Zhu, W. Z., & Liu, C. (2019). Neonate and infant brain development from birth to 2 years assessed using MRI-based quantitative susceptibility mapping. *NeuroImage*, *185*, 349–360.